Layer-by-layer generation of optimized joint trajectory for multi-axis robotized additive manufacturing of parts of revolution

Maxime Chalvin, Sébastien Campocasso, Vincent Hugel, Thomas Baizeau

Layer-by-layer generation of optimized joint trajectory for multi-axis robotized additive manufacturing of parts of revolution

Maxime Chalvin[a,*], Sébastien Campocasso[a], Vincent Hugel[a], Thomas Baizeau[b]

[a] *Université de Toulon, COSMER, Toulon, France*
[b] *Poly-Shape, 235 Rue des Canesteu, ZI la Gandonne, Salon de Provence, France*

Abstract

This work focuses on additive manufacturing by Directed Energy Deposition (DED) using a 6-axis robot. The objective is to generate an optimized trajectory in the joint space, taking into account axis redundancy for parts of revolution produced with a coaxial deposition system. To achieve this goal, a new layer-by-layer method coupled with a trajectory constrained optimization is presented. The optimization results are theoretically compared to a non-optimized trajectory and a point-by-point optimized trajectory. The layer-by-layer generation of optimized trajectories is validated experimentally on a 6-axis robot using a PLA extrusion system. Experimental results show that the layer-by-layer trajectory optimization strategy applied to parts of revolution provides better geometrical accuracy while improving the efficiency of the manufacturing device compared to non-optimized solutions.

Keywords: Additive manufacturing, Multi-axis direct deposition, Redundancy-based trajectory optimization, Layer-by-layer motion planning

Nomenclature

Δ_{layer}	Distance between two consecutive layers used to define the path (mm)
c	Maximum chord error (mm)
$\overrightarrow{b}$	Local build direction vector
q_j	Position of the j^{th} axis (°)
$\underline{\mathbf{q}}$	Joint coordinate vector = $[q_1, q_2, q_3, q_4, q_5, q_6]$
$q_{j_{min}}$	Minimal position of the j^{th} axis (°)
$q_{j_{max}}$	Maximal position of the j^{th} axis (°)
$q_{j_{mean}}$	Average position of the j^{th} axis: $\frac{q_{j_{max}}+q_{j_{min}}}{2}$ (°)
Δ_{q_j}	Stroke of the j^{th} axis: $q_{j_{max}} - q_{j_{min}}$ (°)
$\Phi\left(\underline{\mathbf{q}}\right)$	Scalar objective function
$\underline{\mathbf{\Psi}}\left(\underline{\mathbf{q}}\right) \leq \underline{0}$	Inequality constraint
$\underline{\underline{\mathbf{J}}}\left(\underline{\mathbf{q}}\right)$	Jacobian matrix of the robot

In this document, spatial 3D-vectors are denoted as $\overrightarrow{X}$, whereas the other vectors as $\underline{\mathbf{X}}$ and the matrices as $\underline{\underline{\mathbf{X}}}$.

1. Introduction

Additive manufacturing is a promising technology for the industry because of its flexibility and speed of implementation for the manufacture of single parts or even small series that can be used directly [1, 2]. However, the size of these parts is sometimes not compatible with the industrial requirements [3, 4]. For this reason, Directed Energy Deposition (DED) technologies have been developed to produce near net shape blanks with larger dimensions. Even if these blanks are not directly usable in a mechanical system, less machining is required to produce the final part, which then reduces the cost compared to a traditional manufacturing sequence [3, 5].

Nevertheless, geometries with cantilevered areas remain difficult to produce with additive manufacturing technologies. To perform the manufacturing of this kind of geometries, a support material is generally required [6]. This support material, in addition to being time consuming and useless material for the final part, can be difficult to remove. To achieve additive manufacturing

*Corresponding author

without support for cantilevered parts, multi-axis manufacturing strategies have been developed [7, 8, 9]. These strategies allow manufacturing by tilting the deposition system [10], the part [11] or both [12, 13] to always have material under the deposition point and thus avoid the collapse of the material. The manufacturing device used for multi-axis additive manufacturing is then composed of a deposition system coupled with a 5-axis CNC [14, 15] or a 6-axis robot [3, 16] with or without additional axes such as a positioner or a linear axis.

In the case of a coaxial deposition system, a multi-axis trajectory requires a minimum of five machine axes to be executed. When using a 6-axis robot, whether or not coupled with a 2-axis positioner or a linear axis, there is at least one axis redundancy. This redundancy can be used to improve the robot movement, in order to move away from the joint limits [17, 18, 19], increase the manipulability [20, 21, 22], avoid singularities [17, 23], minimize joint displacements [22, 24], avoid obstacles [18, 20], or improve the robot stiffness [25].

For multi-axis additive manufacturing, the working area can be relatively small, due in particular to a gas shielding system [14]. This small workspace does not necessarily allow the robot to work in a good joint configuration. The configuration of the manufacturing device is then constrained and can lead to difficulties throughout the manufacturing process, such as exceeding the limits of the joint axes, crossing singularity zones or exceeding maximal joint speed.

This article presents a new layer-by-layer generation of trajectories using a constrained optimization strategy. This method is applied to the manufacturing of thin-walled overhanging parts of revolution on an additive manufacturing device with limited working space. The optimization uses different techniques developed for industrial robotics while taking into account the material deposition process. First, a state of the art of multi-axis trajectory generation and exploitation of axis redundancies to improve robot motion is presented in Section 2. Then, the experimental device and the setup are presented in Section 3. Section 4 describes the layer-by-layer optimization process under constraints. Section 5 is devoted to the simulation of the optimization process applied to the manufacturing of a hollow half-sphere and compared to a point-by-point optimization. Finally, an experimental validation through three case studies is carried out in Section 6 to validate the optimization concept.

2. State of the art

2.1. Path planning and build-direction calculation

To perform multi-axis additive manufacturing on thin-walled parts of revolution, a manufacturing trajectory must be defined. This trajectory is composed of a path and a build-direction. The path is defined as the curve followed by the deposition tool and the build-direction can be global for a layer [7, 26] or local for each point of the path [27, 28, 29].

The example used to define the path and the build-directions is a hollow half-sphere with a radius of 45 mm, as shown in Figure 1. This geometry was chosen because of an increasing overhang and a top closure which illustrate the different issues encountered in multi-axis additive manufacturing [6, 12, 30]. To generate the geometry, a 2-D generating curve is rotated about an axis, as explained in Figure 1.

Iso-height Z-level path planning. A first method used to generate the path is based on a classical Z-level decomposition with intersection planes spaced apart from Δ_{layer}. The intersections between the planes and the part give the several layers [13]. The number of points per layer is calculated according to a given chord error c.

If the distance between the planes is set to Δ_{layer}, the actual distance between the layers is different and increases with the overhang. This increase creates a surface condition called the staircase effect [31, 32, 33] and can lead to deposition issues. The deposition system can accept a variation in the distance between two consecutive layers ; plus or minus 20 % if welding technologies are used with fixed deposition conditions [34, 35]. However, such variations can have an impact on the mechanical characteristics [26, 36]. Too great a distance

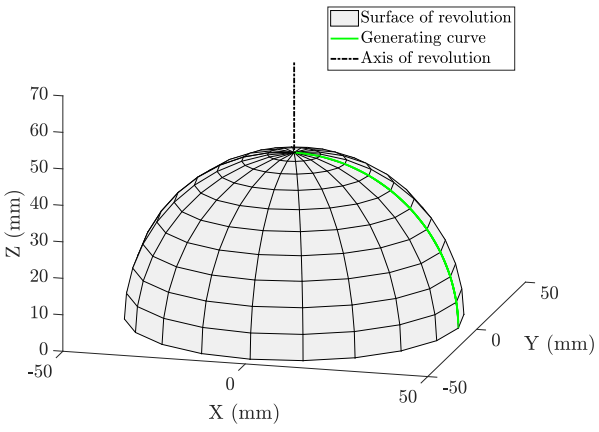

Figure 1: Sphere obtained from the rotation of a generating curve about an axis

between layers can also lead to a deposit defect, such as a workpiece collapse [28] or weld failure [34, 37] if welding technology is used.

Variable height Z-level path planning. Another method to decompose a geometry is to use a Z-level decomposition with a variable distance between the planes [31, 38, 39]. This method decreases the staircase effect and the deposition issues in the cantilevered areas. The variable distance is set by assuming, for a sufficiently low value of Δ_{layer}, that the distance between two layers is equivalent to the curvilinear abscissa calculated on the generating curve between these two layers. The distance between two planes is calculated so that the curvilinear abscissa between two successive layers is equal to Δ_{layer}. The staircase effect is so reduced or even non-existent and the risk of deposit failure may be reduced [31].

Build-direction. To perform multi-axis additive manufacturing, the definition of the build-direction is essential [12]. For best manufacturing performances, a local build-direction - a vector defined at each point of the path - is preferred [27, 29]. This local build-direction vector $\overrightarrow{b}$ is defined as normal to the path and tangent to the surface [28].

Since the definition of the surface is based on a 2-D generating curve rotating about an axis, the first build-direction of a layer can be calculated tangent to this line in the plane containing it [40], in order to be tangent to the surface and normal to the path. The other build-directions are calculated by rotating the first one about the rotation axis (Figure 2).

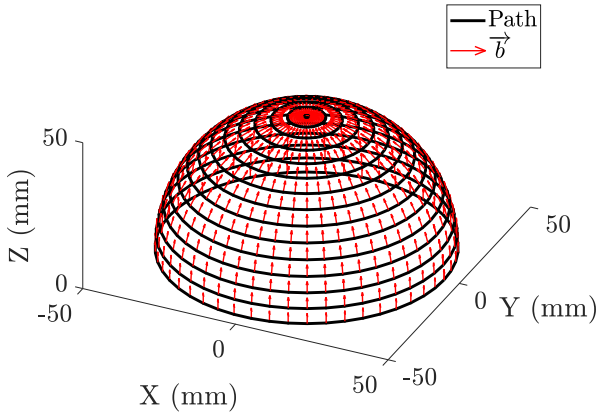

Figure 2: Path planning and local build-directions

2.2. Robot motion improvement through axis redundancy

Optimization strategies that take advantage of the redundancy of robot axes for additive manufacturing work have been little developed to date. Dai et al. [41] proposed jerk minimization in the joint space as well as collision detection based on machine learning, but the manufactured parts were limited to 2D-extruded parts. Dharmawan et al. [22] proposed trajectory optimization guided by an objective function based on dexterity. Sequential Informed Optimization (SIO) was used with initial guesses based on the last state. However, the robot startup configuration must be resolved offline. The results were limited to the simulation of additive manufacturing of non-overhanging thin-walled parts. Both papers were based on a global approach with optimization for each point of the trajectory.

The present work aims in particular to express the objective function and associated constraints in relation with the multiple requirements of additive manufacturing. The following state of the art presents the usual optimization criteria used in industrial robotics, with the objective of selecting the most suitable combination for the optimization of joint movements in the context of multi-axis additive manufacturing.

Getting away from joint limits. In an additive manufacturing device, joint strokes can be an issue. For example if a joint reaches its limit during deposition, this can lead to a manufacturing failure. To describe the distance between the current joint position and the joint limits, many mathematical functions were proposed. A first scalar function, Equation 1, which can be easily implemented was proposed by Liegeois [42]. This method was then improved by Fournier [43], in order to propose a better discrimination between joints in areas close to joint boundaries (Equation 2). Another function was proposed by Klein [44] (Equation 3), in order to better determine the articulations close to their limits, but more difficult than the quadratic forms to implement in a numerical optimization algorithm.

$$\Phi\left(\underline{\mathbf{q}}\right) = \sum_{j=1}^{j=6} \left(\frac{q_j - q_{j_{mean}}}{q_{j_{mean}} - q_{j_{max}}} \right)^2 \tag{1}$$

$$\Phi\left(\underline{\mathbf{q}}\right) = \sum_{j=1}^{j=6} \left(\frac{q_j - q_{j_{mean}}}{\Delta_{q_j}} \right)^2 \tag{2}$$

$$\Phi\left(\underline{\mathbf{q}}\right) = \max \left(\frac{| q_j - q_{j_{mean}} |}{| \Delta_{q_j} |} \right) \quad j \in [1..6] \tag{3}$$

Increasing manipulability and singularity avoidance. Increasing the manipulability of a robot provides a better quality of movement by allowing the robot to move in any spatial direction without being in a singular state [45]. When depositing a layer, a singular state can lead to parasitic movements or stopping of the robot and is therefore undesirable. Increasing the manipulability also allows for better speed tracking, thus ensuring a more continuous robot speed and therefore a constant bead geometry [46] and leading to more homogeneous mechanical properties of the manufactured part [26, 36].

Manipulability can be expressed by a scalar value and a first method consists in measuring the volume of the velocity ellipsoid [45, 47, 48] by using Equation 4.

$$w\left(\underline{\mathbf{q}}\right) = \sqrt{det\left[\underline{\underline{\mathbf{J}}}\left(\underline{\mathbf{q}}\right) \times \underline{\underline{\mathbf{J}}}^{T}\left(\underline{\mathbf{q}}\right)\right]} \tag{4}$$

According to Equation 4, when $w\left(\underline{\mathbf{q}}\right)$ is zero, the robot is in a singular position, whereas when $w\left(\underline{\mathbf{q}}\right)$ is maximal, the robot is in the best areas of manipulability. Since it is easier to minimize a scalar function in numerical optimization, the Equation 4 cannot be used to increase manipulability. The function given in Equation 5 is generally preferred in the implementation of the optimization process to avoid the use of large numerical values. The best areas of manipulability are thus for $\Phi\left(\underline{\mathbf{q}}\right)$ minimum and singularity areas for $\Phi\left(\underline{\mathbf{q}}\right)$ infinite.

$$\Phi\left(\underline{\mathbf{q}}\right) = \frac{1}{\sqrt{det\left[\underline{\underline{\mathbf{J}}}\left(\underline{\mathbf{q}}\right) \times \underline{\underline{\mathbf{J}}}^{T}\left(\underline{\mathbf{q}}\right)\right]}} \tag{5}$$

The manipulability of a robot can also be estimated as proposed by Souissi et al. [49] by quantifying the condition number of the Jacobian matrix using Equation 6. Thus, for a given Cartesian trajectory, the smaller $\Phi\left(\underline{\mathbf{q}}\right)$ is, the less joint motion is required to reach the final position. As for the previous method, when the system is close to a singular state, $\Phi\left(\underline{\mathbf{q}}\right)$ tends towards infinity. Since a singularity state corresponds to an infinite value of $\Phi\left(\underline{\mathbf{q}}\right)$, optimizing manipulability also means avoiding singularities.

$$\begin{aligned} &\Phi\left(\underline{\mathbf{q}}\right) = \frac{\sigma_{min}}{\sigma_{max}} \\ &\sigma_{min} = \sqrt{\min \underline{\boldsymbol{\lambda}}} \\ &\sigma_{max} = \sqrt{\max \underline{\boldsymbol{\lambda}}} \\ &\underline{\boldsymbol{\lambda}} : \text{eigen values of } \underline{\underline{\mathbf{J}}}\left(\underline{\mathbf{q}}\right) \times \underline{\underline{\mathbf{J}}}^{T}\left(\underline{\mathbf{q}}\right) \end{aligned} \tag{6}$$

Minimizing joint movements. Minimizing the robot's joint movements can reduce joint speeds, and, indirectly, joint jerk, thus reducing vibrations and increasing the robot's accuracy [22], which can be beneficial for multiple bead stacking, especially for narrow width beads. This can be done by quantifying joint displacements during manufacturing. To quantify the joint displacements, the total movement of each axis is calculated and a weighting α_j is applied to each axis. These weights, positive or equal to zero, are used to control the mobility of the different axes during manufacturing. The higher the value of α_j, the less the j^{th} axis will move during manufacturing. The mathematical function used to optimize joint motion is described in Equation 7.

$$\begin{aligned} &\Phi\left(\underline{\mathbf{q}}\right) = \sum_{i=2}^{i=N} \sum_{j=1}^{j=6} \alpha_j \cdot \left(q_{i,j} - q_{i-1,j}\right)^2 \\ &N : \text{number of trajectory points} \\ &\alpha_j \geq 0 : \text{weighting of the } j^{th} \text{ axis} \end{aligned} \tag{7}$$

With respect to the state of the art described above, the three main contributions of this paper are as follows:

- The concept of layer-by-layer trajectory optimization,
- The specific combination of the objective function and associated constraints to take advantage of axis redundancy,
- The application of trajectory optimization to the actual manufacturing of parts of revolution with overhangs, leading to a better quality compared with standard manufacturing trajectory.

3. Device and setup

The manufacturing device is composed of a 6-axis Fanuc ARC Mate 120*i*C robot coupled to a vertical PLA deposition system designed to minimize the collisions with the part or the robot during manufacturing (Figure 3). Table 1 gives some characteristics of the robot axes.

The manufacturing configuration is a mobile building platform on which the part is manufactured and a fixed extrusion system. This allows to produce cantilevered geometries with the influence of gravity to be fixed during the manufacturing process.

Speed control. If the robot motion speed is managed in a conventional way (i.e. the speed is calculated in relation to a point fixed on the robot's terminal axis), the speed at the deposition point - which is the spatial point where the material emerges from the deposition tool - depends on the linear and rotational speeds at the point controlled by the robot and the distance between the deposition point and the controlled point. To avoid this issue, the travel speed is managed with the Fanuc RTCP (Remote Tool Center Point) function. This function controls the path and speed of the robot relative to a fixed point in Cartesian space.

Deposition system. The deposition system uses a PLA wire with a nozzle diameter of 1 mm. In addition to reducing the thermal effects on the part, the use of polymers is easier to deposit and allows fewer problems in case of collision between the part and the nozzle: the deposition nozzle being at high temperature, in case of collision, it will pass through the part instead of being damaged. The robot's moving speed used for PLA deposition, 6 mm/s, is close to the maximum encountered for DED using wire [3, 50]. This allows the robot to operate under similar dynamic conditions. However, some metal deposition issues are avoided, such as: management of the deposition temperature [51], distortion of parts during manufacturing [52] and management of deposition starts and stops [53, 54].

Axis	Stroke (°)	Max speed ($° \cdot s^{-1}$)
1	± 185	195
2	± 160	175
3	± 273	180
4	± 200	360
5	± 135	360
6	± ∞	550

Table 1: Characteristics of the Fanuc ARC Mate 120 *i*C joints

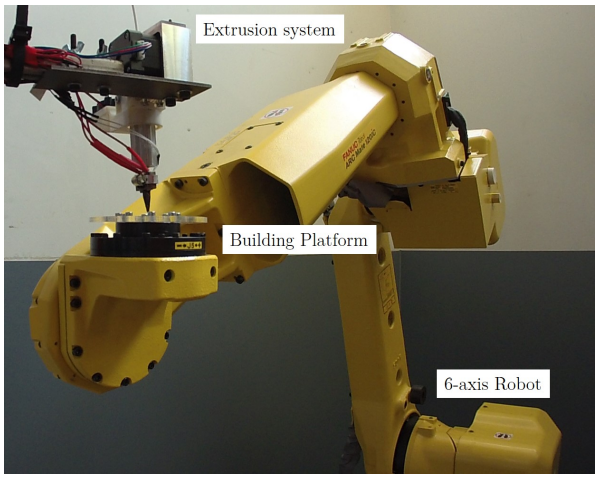

Figure 3: Additive manufacturing device located at the University of Toulon

4. Methods

In this section, the methods developed to manufacture a thin-walled part of revolution are presented. The flowchart in Figure 4 summarizes the entire process chain, divided into six main steps from the geometric model to manufacturing. The third step concerning the layer-by-layer optimization process will be detailed in the following subsections.

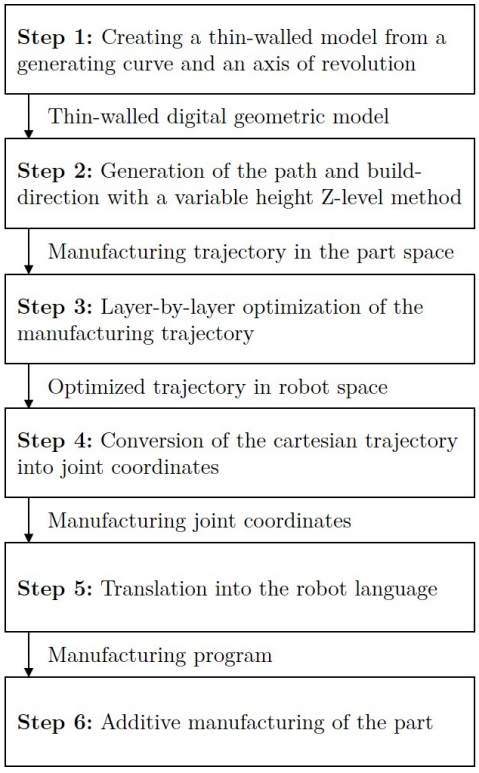

Figure 4: General flowchart of the proposed approach

4.1. Optimization variable

In the case of Directed Energy Deposition (DED) technologies with a material feeding that is collinear with the energy supply, rotation about the deposition tool axis has no effect on the deposition process [55, 56, 57].

To perform multi-axis additive manufacturing, the angle between the local build-direction vector and the deposition tool axis must be fixed. In the present case the build-direction vector is collinear with the deposition tool axis and also with $\overrightarrow{Z_{Robot}}$.

The layer-by-layer optimization is based on the robot Inverse Geometric Model (IGM). The trajectory followed by the point controlled by the robot is described by the following set of variables $[X, Y, Z, R_X, R_Y, R_Z]_{Robot}$, where:

- $[X, Y, Z]_{Robot}$ denotes the Cartesian coordinates of each point expressed into the robot's coordinate system,
- $[R_X, R_Y, R_Z]_{Robot}$ denotes the orientation parameters of the build-direction vector.

The convention used for the $[R_X, R_Y, R_Z]_{Robot}$ orientation parameters is the Bryant convention [58] where the first rotation is about $\overrightarrow{X_{Robot}}$, the second about $\overrightarrow{Y'_{Robot}}$ and the third about $\overrightarrow{Z''_{Robot}}$.

By setting the build direction collinear with the deposition tool axis, the workpiece being manufactured is free to rotate about the deposition tool axis (Figure 5). Since the R_Z parameter is directly related to the degree of freedom corresponding to the rotation about the deposition tool axis, an optimization of the joint movement based on this parameter is possible. However, since the orientation of the part in the robot axes system is described with three orientation parameters $[R_X, R_Y, R_Z]_{Robot}$, they must be extracted from the build-direction vectors in order to be used in the IGM. Different cost and constraint functions must also be defined in order to perform the path optimization.

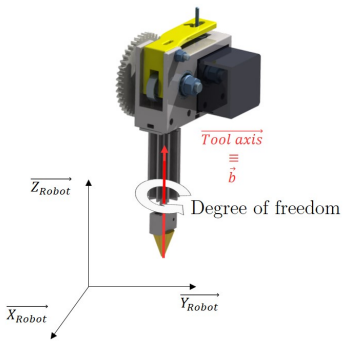

Figure 5: Rotation about the deposition $\overrightarrow{\text{Tool axis}}/\vec{b}$

4.2. Definition of the orientation parameters

To extract the orientation parameters with the Bryant convention, the build-direction vector is defined in the part coordinate system as:

$$\vec{b} = \begin{bmatrix} b_X \\ b_Y \\ b_Z \end{bmatrix}_{Part} \tag{8}$$

The transformation matrix between the robot and the part coordinates system is:

$$\begin{aligned} &\underline{\underline{\mathbf{M}_{Robot \to Part}}} = \underline{\underline{\mathbf{M}_{R_X}}} \times \underline{\underline{\mathbf{M}_{R_Y}}} \times \underline{\underline{\mathbf{M}_{R_Z}}} \\ &\text{with} \\ &\underline{\underline{\mathbf{M}_{R_X}}} = \begin{bmatrix} 1 & 0 & 0 \\ 0 & \cos R_X & -\sin R_X \\ 0 & \sin R_X & \cos R_X \end{bmatrix} \\ &\underline{\underline{\mathbf{M}_{R_Y}}} = \begin{bmatrix} \cos R_Y & 0 & \sin R_Y \\ 0 & 1 & 0 \\ -\sin R_Y & 0 & \cos R_Y \end{bmatrix} \\ &\underline{\underline{\mathbf{M}_{R_Z}}} = \begin{bmatrix} \cos R_Z & -\sin R_Z & 0 \\ \sin R_Z & \cos R_Z & 0 \\ 0 & 0 & 1 \end{bmatrix} \end{aligned} \tag{9}$$

As previously described in Section 4.1, in the present case, the build direction vector is collinear with the deposition tool axis and at the same time with $\overrightarrow{Z_{Robot}}$. This equality is transcribed into the Equation 10:

$$\overrightarrow{Tool\ axis} \times \underline{\underline{\mathbf{M}_{Robot \to Part}}} = \overrightarrow{Z_{Robot}} \times \underline{\underline{\mathbf{M}_{Robot \to Part}}} = \vec{b} \tag{10}$$

From Equation 10, it is possible to express the orientation parameters with the build-direction coordinates:

$$\begin{aligned} \begin{bmatrix} b_X \\ b_Y \\ b_Z \end{bmatrix}^T &= \begin{bmatrix} 0 \\ 0 \\ 1 \end{bmatrix}^T \times \underline{\underline{\mathbf{M}_{R_X}}} \times \underline{\underline{\mathbf{M}_{R_Y}}} \times \underline{\underline{\mathbf{M}_{R_Z}}} \\ &= \begin{bmatrix} \sin R_X \cdot \sin R_Z - \cos R_X \cdot \sin R_Y \cdot \cos R_Z \\ \sin R_X \cdot \cos R_Z + \cos R_X \cdot \sin R_Y \cdot \sin R_Z \\ \cos R_X \cdot \cos R_Y \end{bmatrix}^T \end{aligned} \tag{11}$$

An infinite combination of $[R_X, R_Y, R_Z]_{Robot}$ is possible by rotating the part about the deposition tool axis. R_X and R_Y must also be extracted from the $\vec{b}$ coordinates and from R_Z. The R_Z parameter will be optimized so that the Cartesian coordinates can be used in the IGM model. The Equations 12 and 13 giving R_X and R_Y from

R_Z and $\overrightarrow{b}$ are obtained by multiplying the Equation 11 by $inv(\underline{\underline{\mathbf{M}_{R_Z}}})$:

$$\begin{bmatrix} b_X \\ b_Y \\ b_Z \end{bmatrix}^T \times inv(\underline{\underline{\mathbf{M}_{R_Z}}}) = \begin{bmatrix} 0 \\ 0 \\ 1 \end{bmatrix}^T \times \underline{\underline{\mathbf{M}_{R_X}}} \times \underline{\underline{\mathbf{M}_{R_Y}}} \tag{12}$$

$$\begin{bmatrix} b_X \cdot \cos R_Z - b_Y \cdot \sin R_Z \\ b_Y \cdot \cos R_Z + b_X \cdot \sin R_Z \\ b_Z \end{bmatrix}^T = \begin{bmatrix} -\cos R_X \cdot \sin R_Y \\ \sin R_X \\ \cos R_X \cdot \cos R_Y \end{bmatrix}^T \tag{13}$$

With the Equation 13, it is possible to express the R_X and R_Y parameters according to the $\overrightarrow{b}$ coordinates and the R_Z parameter (Equations 14, 15).

$$\begin{aligned} R_X &= \text{atan2}\,(S_X, C_X) \\ &\quad \text{with} \\ S_X &= b_Y \cdot \cos R_Z + b_X \cdot \sin R_Z \\ C_X &= \sqrt{(b_X \cdot \cos R_Z - b_Y \cdot \sin R_Z)^2 + b_Z^2} \end{aligned} \tag{14}$$

$$\begin{aligned} R_Y &= \text{atan2}\,(S_Y, C_Y) \\ &\quad \text{with} \\ S_Y &= -(b_X \cdot \cos R_Z - b_Y \cdot \sin R_Z) \\ C_Y &= b_Z \end{aligned} \tag{15}$$

The Cartesian coordinates $[X, Y, Z]_{Robot}$ of the trajectory are known and the orientation coordinates R_X and R_Y are calculated according to the build-direction vector coordinates for any value of R_Z. In addition, since the IGM is known, for each point of the trajectory, the joints coordinate vector $\mathbf{q}$ will only depend on the R_Z parameter. It is therefore possible to implement a numerical function of R_Z for layer-by-layer optimization.

4.3. Layer-by-layer trajectory optimization

Trajectory optimization can allow manufacturing even in a constrained device configuration, where a non-optimized trajectory would fail due to a singular state or joint over-travel. For example, the production of a sphere with a constant R_Z causes an over-travel of the axis No.5, as shown in Figure 7. Optimizing a path can enable manufacturing by staying within axis limits and, furthermore, reducing axis movements, accelerations or staying below the maximum speed of each axis to obtain better quality parts.

The algorithm used for the optimization is that of the interior-point through Matlab "fmincon" function, with the following parameters:

- Maximum number of iterations: 1000 (never reached),
- Termination tolerance on the function value: 1.10^{-8},
- Termination tolerance on the current point: 1.10^{-8},
- No parallel computing.

The principle of the layer-by-layer optimization process is to optimize the trajectory of each layer independently of each other. To do this, an optimization variable is introduced for each layer. A $(n+1)$-dimension vector $\underline{A_{L,n}}$ is used to define the R_Z parameter by a n degrees polynomial function, Equation 16. This polynomial definition of the R_Z parameter allows a continuous variation of the R_X, R_Y and R_Z parameters along a layer.

$$R_{Z_{L,i}} = a_{L,n} \cdot \theta_{L,i}^n + a_{L,n-1} \cdot \theta_{L,i}^{n-1} + ... + a_{L,0} \tag{16}$$

with

$\underline{A_{L,n}} = \begin{bmatrix} a_{L,n} \\ a_{L,n-1} \\ ... \\ a_{L,0} \end{bmatrix}$: Variable vector for the layer L

$\theta_{L,i}$: Cylindrical coordinates of the point i of the layer L

$\theta_{L,i} = \text{atan}\left(\frac{Y_{L,i}}{X_{L,i}}\right)$

$Y_{L,i}$ and $X_{L,i}$ expressed into the part coordinate system

The use of a manipulability objective function for layer-by-layer optimization is not appropriate because the manipulability value can be highly variable along a layer. In some cases, the optimization algorithm may focus on a specific point with the highest manipulability value while the other manipulability values are negligible compared to the first one.

The selected objective function allows a minimization of the joint displacements (Equation 17) with a weighting equal to the inverse of the stroke of each axis. Furthermore, an inequality constraint to stay within the axis limits is defined and described in Equation 18. An inequality constraint is also defined to avoid singularities. This inequality constraint is necessary because singularity avoidance is not handled by the cost function used to minimize the joint displacement. The function that has been implemented is extrapolated from the manipulability index (Equation 6) proposed by Souissi et

al. [49] and is described in Equation 19. The trajectory optimization process for a layer L is summarized in Figure 6.

$$\Phi\left(\underline{\mathbf{q}}(R_Z)\right) = \sum_{i=2}^{i=N_L}\sum_{j=1}^{j=6}\alpha_j \cdot \left(q_{i,j} - q_{i-1,j}\right)^2$$
$$N_L : \text{number of points of the L}^{\text{th}}\text{ layer} \quad (17)$$
$$\alpha_j = \frac{1}{\Delta_{q_j}}$$

$$\underline{\boldsymbol{\Psi}}\left(\underline{\mathbf{q}}(R_Z)\right) = [\psi_1..\psi_7]$$
$$\psi_j = \max_i\left(\left(\frac{q_j - q_{j,mean}}{\Delta_{q_j}}\right)^2 - \left(\frac{1}{2}\right)^2\right) \quad j \in 1,6 \quad (18)$$
$$\psi_7 = \max_i\left(\left(\frac{\sigma_{min}}{\sigma_{max}}\right)_i - \psi_{max}\right) \quad i \in 1, N_L \quad (19)$$

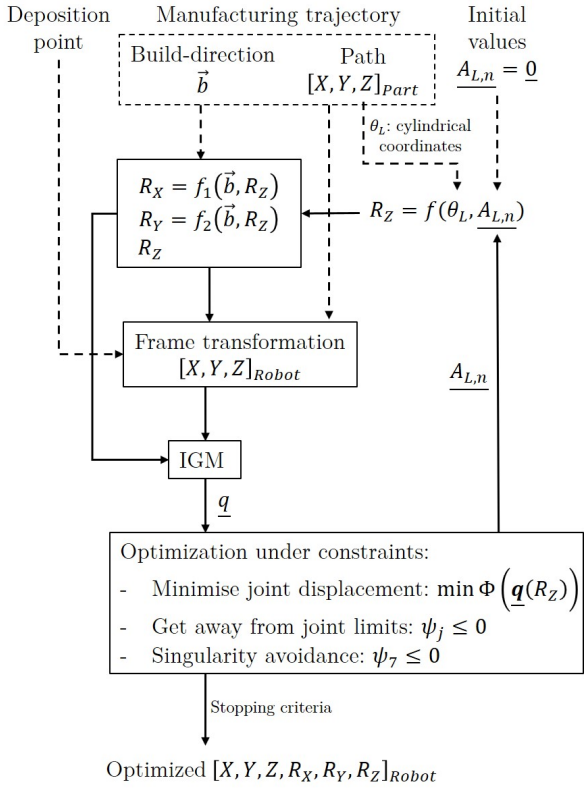

Figure 6: $\underline{A_{L,n}}$ optimization for a layer L

5. Simulation results

5.1. Layer-by-layer joint optimization

The layer-by-layer optimization method was applied for the manufacture of a hollow half-sphere with the manufacturing device described in Section 3 placed in a constrained configuration. To adjust the singularity avoidance constraint (described in Equation 19), ψ_{max} was empirically chosen as the value of one quarter of the manipulability calculated for each point in the case of R_Z constant.

Since the computation time is directly related to the degree of the polynomial function, it is important to select the best one in order to have the best ratio between results and computation time. As the optimization is applied to parts of revolution and as the R_Z parameter is expressed in terms of cylindrical coordinates, the degree of the polynomial function should be $n = 1$. For more complex geometries, this size may be larger for better results due to a possible non-linear variation of R_Z. Several tests were performed for a degree of the polynomial function ranging from $n = 1$ to $n = 3$. The results obtained for the different values of n are identical and can be seen in Figure 7 (the curves are superimposed). The computation time for the optimization with $n = 1$ was about 92 s (CPU Intel Core i7 @ 2.60 GHz with 16 Gb RAM).

The solution of positioning axes No.1 to No.5 for each layer and having a continuous rotation of the axis No.6 seems obvious but is obtained here automatically. This solution should allow a better layer circularity with respect to a non-optimized trajectory. In addition, as the axis which is most stressed is the closest to the deposition tool, it also allows to minimize the impact of the positioning errors of the different axes on the final result.

5.2. Comparison with a point-by-point optimization

For the point-by-point trajectory optimization process, the optimization variable is directly R_Z which is determined for each point of the trajectory. The same optimization and constraint functions were used. The result can be seen in Figure 8.

Like layer-by-layer optimization, point-by-point allows the axes to stay within their limits and avoid singularity zones. However, some abrupt joint movements do occur. These sudden variations are undesirable not only because the robot may not be able to follow the instructions due to its dynamics, but also because abrupt

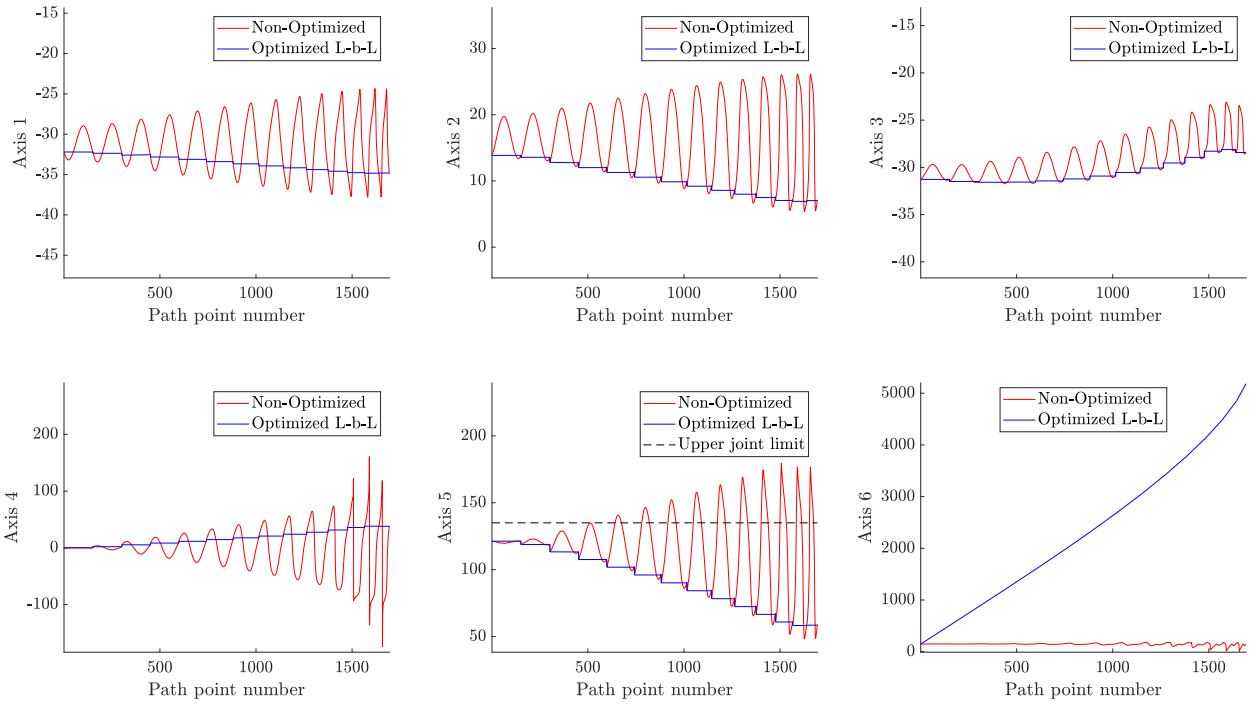

Figure 7: Layer-by-layer optimization. Application to a hollow half-sphere. Δ_{layer} = 5 mm, c = 0.01 mm

movements can impact the deposit if it is not yet solidified. In addition, strong jerk can affect long-term reliability.

The computation time for point-by-point optimization was about 307 s which is an increase of 234 % compared to layer-by-layer optimization.

In this case, point-by-point optimization is not suitable.

5.3. Conclusions of the simulation analysis

Compared with a point-by-point and non-optimized trajectory, layer-by-layer optimization results in smoother joint behavior that can improve the quality of the part. This behavior is due to a continuous and differentiable manufacturing trajectory for each layer. It should be noted that since the different layers are treated independently, the joint movement between two consecutive layers is not taken into account. Here, this movement is as small as possible. However, this transition can be used to improve the additive manufacturing process. In the case of the use of WAAM technology, the transition can be used to cool the workpiece. During the waiting time, it is also possible to reconfigure the robot to work in better joint conditions (by increasing the distance from singularity areas, staying within axis limits while having the same type of robot movement), to clean the welding nozzle, or even to machine the last layer deposited and continue the deposition to manufacture the next layer (hybrid manufacturing).

6. Experimental results and analysis

To validate the layer-by-layer optimization method, three case studies are detailed in this section. The manufacturing of these parts on the experimental device with a constrained configuration demonstrates the attractiveness of layer-by-layer trajectory optimization in cases where it is not possible to manufacture without it. Moreover, a geometrical inspection of the spheres produced with and without layer-by-layer optimized trajectories (in a robot configuration that allows it) is finally proposed to compare the quality of the parts.

For the different case studies, in order to ensure that the robot movement is carried out with the optimized trajectory, the robot is controlled with joint coordinates. The manufacturing parameters used for the trajectory and the deposit are listed in Table 3. The manufacturing device configuration is as follows:

- Robot configuration:

  Shoulder: Top,

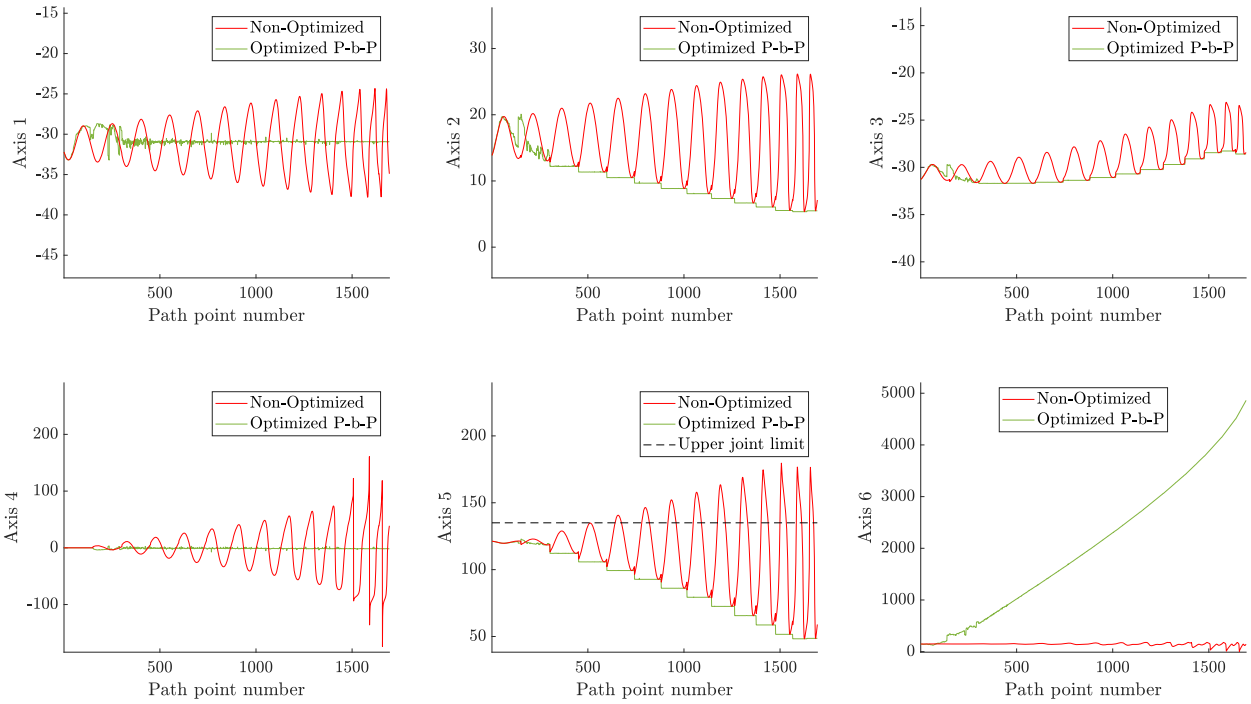

Figure 8: Point-by-point optimization. Application to a hollow half-sphere. Δ_{layer} = 5 mm, c = 0.01 mm

Elbow: Up,

Wrist: Flip,

- Cartesian coordinates and orientations of the deposition point in the robot coordinate system: $[1045.747, -630.155, 653.167, 0, 0, 0]_{Robot}$,
- Building platform dimensions: 113 mm diameter, 5 mm thick. Material: plexiglass.

For each case study, the manufacturing on the constrained device was only possible with the optimized manufacturing trajectory (Figure 10).

To verify whether an optimized trajectory gives similar or better results that a non-optimized path, the robot configuration was modified to be able to perform the sphere manufacturing with and without the optimized path. The spheres produced were geometrically inspected.

6.1. Case studies

Sphere. The first case study is the one used to define the manufacturing path and the different build-directions: a hollow half-sphere, shown in Figure 9a. This geometry was chosen, in addition to the reasons mentioned in Section 2.1, for the following reasons:

- Closed surface,
- High cantilevered areas close to the top,
- Thin wall,
- Single radius of curvature: positive,
- Easy geometry characterization.

The equation of the theoretical curve used to define the sphere is the following:

$$\begin{aligned} x &= \sqrt{R_0^2 - z^2} \\ R_0 &= 45 \text{ mm} \\ z &\in [0 : R_0] \end{aligned} \tag{20}$$

In order to prevent collisions between the workpiece and the deposition tool during the manufacture of this part, the build-direction vectors on top of the geometry were tilted. The angle of inclination was calculated as a function of the nozzle angle. The tilted build-direction vectors are visible in Figure 9a (blue arrows).

Laval nozzle. The second case study is a Laval nozzle (Figure 9b). The characteristics of this geometry are:

- Open surface,
- Overhang areas,

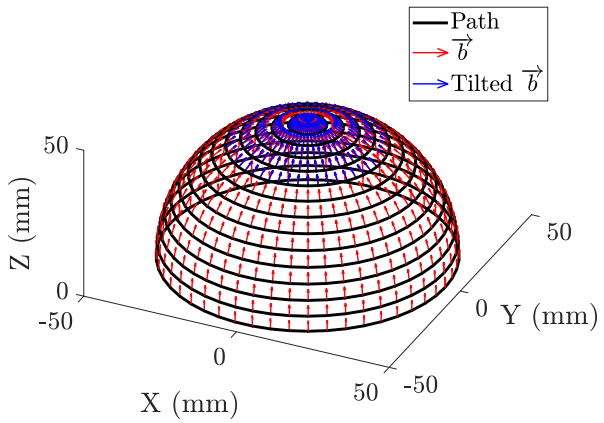

(a)

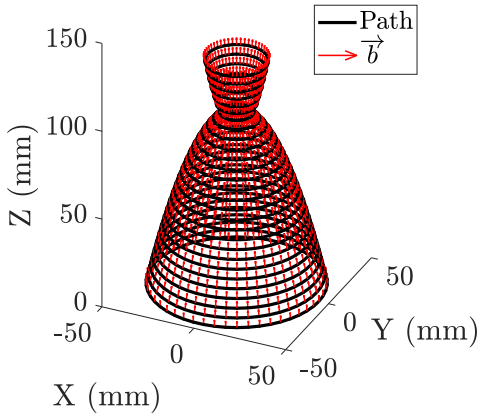

(b)

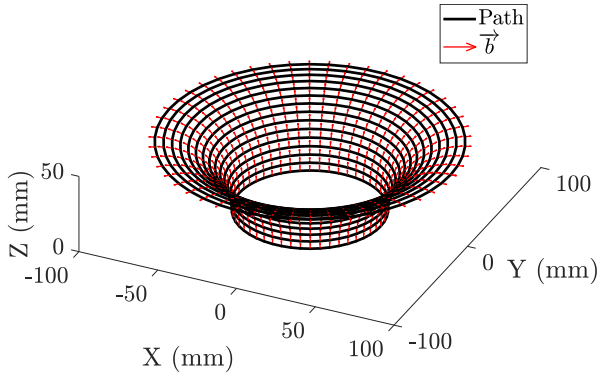

(c)

Figure 9: Path and local build-directions: a: Sphere ; b: Laval nozzle ; c: Intake funnel

- Thin wall,
- Double radius of curvature: negative and positive.

The equation of the theoretical curve used to define this geometry is Equation 21. The parameters ρ and θ were derived from those given by Boccaletto [59].

$$\begin{aligned} x = & \sqrt{(z-\theta)\cdot 2\cdot\rho} \\ \text{for } z \in & [0:96.5] \\ \rho = & -10 \\ \theta = & 100 \\ \text{for } z \in &]96.5:128] \\ \rho = & 3 \\ \theta = & 85 \end{aligned} \tag{21}$$

Intake funnel. The third case study is a geometry similar to the shape of an intake funnel (Figure 9c). This geometry has the following characteristics:

- Open surface,
- Important overhang,
- Thin wall,
- Single radius of curvature: negative.

The equation of the theoretical curve used to define the intake funnel is Equation 22.

$$\begin{aligned} & x = 2\cdot R_0 - \sqrt{R_0^2 - z^2} \\ & R_0 = 45 \text{ mm} \\ & z \in [0 : R_0] \end{aligned} \tag{22}$$

6.2. *Optimized and non-optimized trajectories comparison*

To carry out manufacturing with the non-optimized trajectory, the robot was freed from any constraint by moving the deposition system to a higher position while having the same joint configuration. The new Cartesian coordinates and orientation of the deposition point in the robot space are: $[988.057, -733.138, 1104.885, 0, 0, 0]_{Robot}$.

A Zeiss coordinate measuring machine with Calypso software was used to inspect the parts. The spherical defect was quantified with a helical strategy: 10 revolutions from 10 mm to 40 mm high and one point measured every 0.5 mm. Three circularity defects were also measured, one at the base of the geometry (15 mm), one in the middle (25 mm) and one at the top (35 mm)

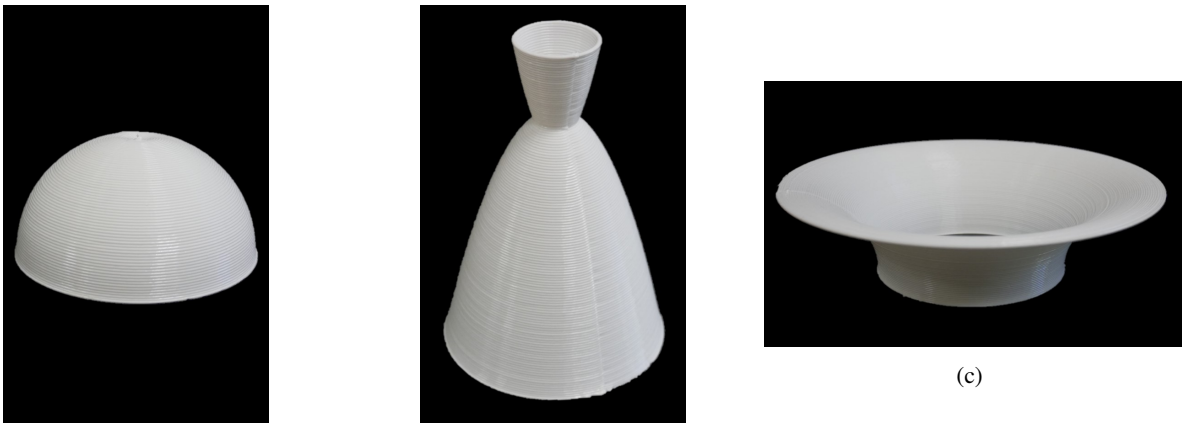

(a) (b) (c)

Figure 10: Experimental results: a: Sphere ; b: Laval nozzle ; c: Intake funnel

	Optimized	Non-optimized	Gap
Spherical defect (mm)	0.326	0.841	+ 158 %
Standard deviation (mm)	0.019	0.149	+ 684 %
Circularity defect - bottom (mm)	0.226	0.422	+ 87 %
Standard deviation (mm)	0.029	0.107	+ 269 %
Circularity defect - middle (mm)	0.227	0.513	+ 126 %
Standard deviation (mm)	0.036	0.048	+ 33 %
Circularity defect - top (mm)	0.319	0.770	+ 141 %
Standard deviation (mm)	0.073	0.038	- 48 %
Power consumption (Wh)	236	251	+6 %

Table 2: Spheres inspection for optimized and non-optimized trajectory

Path parameters		Deposition parameters			
Δ_{layer}	c	Deposition material	Travel Speed (TS)	Wire Feed Speed (WFS)	Extrusion temperature
1 mm	0.01 mm	PLA	6 mm/s	10 mm/s	210 °C

Table 3: Manufacturing parameters for the path and the deposit

with a point measured every 0.5 mm. The characterizations were performed on six spheres: three with an optimized trajectory and three with a non-optimized trajectory. The measured data are given in Table 2.

For each manufacture, the optimized trajectory gives better results in terms of spherical defect and circularity defect. In addition, the optimized trajectory reduces the disparity of the results. This is possible due to the smaller joint displacements during manufacture and because the axis with the highest load i closest to the deposition point. The energy consumption for the optimized path is about 236 Wh and about 251 Wh for the non-optimized path. The manufacturing time is similar for both cases. But even though the energy consumption savings are not significant (-6 % for the optimized trajectory), the optimized trajectory allows less acceleration and less jerk on all axes, which increases the life of the robot joints.

7. Conclusion

In this paper, a numerical layer-by-layer constrained optimization method for multi-axis additive manufacturing of thin-walled parts of revolution has been proposed. This method takes advantage of axis redundancy: a 6-axis robot is used to carry out a manufacturing process requiring only 5 axes. Indeed, the rotation about the deposition tool axis has no effect on the deposition thanks to a coaxial deposition system. The optimization is based on the knowledge of

the manufacturing device: Cartesian coordinates, orientations of the deposition tool and the inverse geometric model of the robot. Compared with a point-by-point or a non-optimized trajectory, the benefits of a layer-by-layer method, based on a polynomial definition of the optimization variable allowing a continuous and differentiable manufacturing trajectory, provides smoother joint behavior and improved manufacturing performance while reducing computation time. In addition, layer-by-layer optimization allows an anticipation of the consideration of the distance from joint limits, to zones of singularity and thus avoids significant movements of the robot during the manufacture of a layer, which could be a source of defects. The independent treatment of the layer also allows other manufacturing operations, such as machining or reconfiguring the device between two layers to improve the manufacturing process.

To validate the optimization method, three case studies were conducted: a sphere, a Laval nozzle and an intake funnel. A path generation method establishing a constant local distance between the layers and a local orientation allowing the manufacture of overhanging parts without support has been detailed. Manufacturing experiments were carried out and showed that, for a constrained device, manufacturing was possible only with an optimized trajectory. In addition, in a configuration allowing manufacturing with and without trajectory optimization, the use of an optimized trajectory, by requesting the axis closest to the deposition point and minimizing joint movements, gives better quality parts. A comparison between the spheres produced with and without optimization shows that those produced with layer-by-layer optimized trajectory have a better geometrical accuracy (sphericity and layer circularity) and less dispersion of the results.

Industrial applications related to this work are mainly related to the aerospace field, as for the manufacture of rocket nozzles [60, 61], fuel tanks or pressure vessels.

Future work will focus on applying layer-by-layer trajectory optimization to more complex geometries, such as tubular geometries [28], with an improvement in the polynomial function used for the optimization variable. A second perspective is a comparison between two configurations of a manufacturing device. Since most of the additive manufacturing devices involving a 6-axis robot are also coupled with a 2-axis positioner, the part and the deposition system are in motion and there are 8 axes increasing axis redundancy. Then, it will be interesting to carry out a comparison between a configuration with a fixed deposition system and a moving part, allowing only small and lightweight parts, and a configuration with a moving deposition system and a moving part, capable of producing larger parts.

Acknowledgments

The authors would like to thank the metropolis Toulon Provence Méditerranée (TPM) for the financial support of the ROBOWAM project as well as the IUT of Toulon for the provision of the premises.

References

[1] E. Atzeni, A. Salmi, Economics of additive manufacturing for end-usable metal parts, The International Journal of Advanced Manufacturing Technology 62 (9-12) (2012) 1147–1155. doi:10.1007/s00170-011-3878-1.

[2] D. S. Thomas, S. W. Gilbert, Costs and cost effectiveness of additive manufacturing, Tech. Rep. NIST SP 1176, National Institute of Standards and Technology (2014). doi:10.6028/NIST.SP.1176.

[3] S. W. Williams, F. Martina, A. C. Addison, J. Ding, G. Pardal, P. Colegrove, Wire + arc additive manufacturing, Materials Science and Technology 32 (7) (2016) 641–647. doi:10.1179/1743284715Y.0000000073.

[4] W. E. Frazier, Metal additive manufacturing: A review, Journal of Materials Engineering and Performance 23 (6) (2014) 1917–1928. doi:10.1007/s11665-014-0958-z.

[5] P. Urhal, A. Weightman, C. Diver, P. Bartolo, Robot assisted additive manufacturing: A review, Robotics and Computer-Integrated Manufacturing 59 (2019) 335–345. doi:10.1016/j.rcim.2019.05.005.

[6] H. Shen, H. Diao, S. Yue, J. Fu, Fused deposition modeling five-axis additive manufacturing: Machine design, fundamental printing methods and critical process characteristics, Rapid Prototyping Journal 24 (3) (2018) 548–561. doi:10.1108/RPJ-05-2017-0096.

[7] D. Ding, Z. Pan, D. Cuiuri, H. Li, N. Larkin, S. van Duin, Automatic multi-direction slicing algorithms for wire based additive manufacturing, Robotics and Computer-Integrated Manufacturing 37 (2016) 139–150. doi:10.1016/j.rcim.2015.09.002.

[8] D. Ding, Z. Pan, D. Cuiuri, H. Li, S. van Duin, Advanced design for additive manufacturing: 3D slicing and 2D path planning, in: I. V. Shishkovsky (Ed.), New Trends in 3D Printing, InTech, 2016, pp. 3–23. doi:10.5772/63042.

[9] Y. Murtezaoglu, D. Plakhotnik, M. Stautner, T. Vaneker, F. J. A. M. van Houten, Geometry-based process planning for multi-axis support-free additive manufacturing, Procedia CIRP 78 (2018) 73–78. doi:10.1016/j.procir.2018.08.175.

[10] J. Ruan, K. Eiamsa-ard, F. Liou, Automatic process planning and toolpath generation of a multiaxis hybrid manufacturing system, Journal of Manufacturing Processes 7 (1) (2005) 57–68. doi:10.1016/S1526-6125(05)70082-7.

[11] D. Kanakanala, Multi axis slicing for rapid prototyping, Ph.D. thesis, Missouri University of Science and Technology (2010).

[12] D. Coupek, J. Friedrich, D. Battran, O. Riedel, Reduction of support structures and building time by optimized path planning algorithms in multi-axis additive manufacturing, Procedia CIRP 67 (2018) 221–226. doi:10.1016/j.procir.2017.12.203.

[13] Y. Ding, R. Dwivedi, R. Kovacevic, Process planning for 8-axis robotized laser-based direct metal deposition system: A case on

building revolved part, Robotics and Computer-Integrated Manufacturing 44 (2017) 67–76. doi:10.1016/j.rcim.2016.08.008.

[14] Y. K. Bandari, S. W. Williams, J. Ding, F. Martina, Additive manufacture of large structures: Robotic or CNC systems, in: Proceedings of the 26th International Solid Freeform Fabrication Symposium, Austin, TX, USA, 2015, pp. 12–14.

[15] L. Ren, T. Sparks, J. Ruan, F. Liou, Integrated process planning for a multiaxis hybrid manufacturing system, Journal of Manufacturing Science and Engineering 132 (2) (2010) 021006. doi:10.1115/1.4001122.

[16] P. A. Colegrove, A. R. McAndrew, J. Ding, F. Martina, P. Kurzynski, S. Williams, System architectures for large scale wire + arc additive manufacture, 10th International Conference on Trends in Welding Research (2016) 5.

[17] J. Gao, Optimal motion planning in redundant robotic systems for automated composite lay-up process, PhD Thesis, Ecole Centrale de Nantes (2018).

[18] L. B. Gueta, J. Cheng, R. Chiba, T. Arai, T. Ueyama, J. Ota, Multiple-goal task realization utilizing redundant degrees of freedom of task and tool attachment optimization, in: 2011 IEEE International Conference on Robotics and Automation, IEEE, Shanghai, China, (2011), pp. 1714–1719. doi:10.1109/ICRA.2011.5980546.

[19] F. Chaumette, T. Marchand, A redundancy-based iterative approach for avoiding joint limits: Application to visual servoing, IEEE Transactions on Robotics and Automation 17 (5) (2001) 719–730. doi:10.1109/70.964671.

[20] R. Menasri, A. Nakib, B. Daachi, H. Oulhadj, P. Siarry, A trajectory planning of redundant manipulators based on bilevel optimization, Applied Mathematics and Computation 250 (2015) 934–947. doi:10.1016/j.amc.2014.10.101.

[21] A. P. Pashkevich, A. B. Dolgui, O. A. Chumakov, Multiobjective optimization of robot motion for laser cutting applications, International Journal of Computer Integrated Manufacturing 17 (2) (2004) 171–183. doi:10.1080/0951192031000078202.

[22] A. G. Dharmawan, S. Padmanathan, Y. Xiong, I. F. Ituarte, S. Foong, G. S. Soh, Maximizing robot manipulator's functional redundancy via sequential informed optimization, in: 2018 3rd International Conference on Advanced Robotics and Mechatronics (ICARM), IEEE, Singapore, (2018), pp. 334–339. doi:10.1109/ICARM.2018.8610834.

[23] V. K. Mehta, B. Dasgupta, A general approach for optimal kinematic design of 6-DOF parallel manipulators, Sadhana 36 (6) (2011) 977–994. doi:10.1007/s12046-011-0057-x.

[24] A. Dolgui, A. Pashkevich, Manipulator motion planning for high-speed robotic laser cutting, International Journal of Production Research 47 (20) (2009) 5691–5715. doi:10.1080/00207540802070967.

[25] B. Gonul, O. F. Sapmaz, L. T. Tunc, Improved stable conditions in robotic milling by kinematic redundancy, Procedia CIRP 82 (2019) 485–490. doi:10.1016/j.procir.2019.04.334.

[26] N. Shamsaei, A. Yadollahi, L. Bian, S. M. Thompson, An overview of Direct Laser Deposition for additive manufacturing; Part II: Mechanical behavior, process parameter optimization and control, Additive Manufacturing 8 (2015) 12–35. doi:10.1016/j.addma.2015.07.002.

[27] Q. Tang, S. Yin, Y. Zhang, J. Wu, A tool vector control for laser additive manufacturing in five-axis configuration, The International Journal of Advanced Manufacturing Technology 98 (5-8) (2018) 1671–1684. doi:10.1007/s00170-018-2177-5.

[28] M. Chalvin, S. Campocasso, T. Baizeau, V. Hugel, Automatic multi-axis path planning for thinwall tubing through robotized wire deposition, Procedia CIRP 79 (2019) 89–94. doi:10.1016/j.procir.2019.02.017.

[29] J. Flores, I. Garmendia, J. Pujana, Toolpath generation for the manufacture of metallic components by means of the laser metal deposition technique, The International Journal of Advanced Manufacturing Technology 101 (5-8) (2019) 2111–2120. doi:10.1007/s00170-018-3124-1.

[30] S. Campocasso, M. Chalvin, A. K. Reichler, R. Gerbers, K. Dröder, V. Hugel, F. Dietrich, A framework for future CAM software dedicated to additive manufacturing by multi-axis deposition, Procedia CIRP 78 (2018) 79–84. doi:10.1016/j.procir.2018.08.314.

[31] W. Ma, W.-C. But, P. He, NURBS-based adaptive slicing for efficient rapid prototyping, Computer-Aided Design 36 (13) (2004) 1309–1325. doi:10.1016/j.cad.2004.02.001.

[32] S. Singamneni, A. Roychoudhury, O. Diegel, B. Huang, Modeling and evaluation of curved layer fused deposition, Journal of Materials Processing Technology 212 (1) (2012) 27–35. doi:10.1016/j.jmatprotec.2011.08.001.

[33] L. Galantucci, F. Lavecchia, G. Percoco, Experimental study aiming to enhance the surface finish of fused deposition modeled parts, CIRP Annals 58 (1) (2009) 189–192. doi:10.1016/j.cirp.2009.03.071.

[34] D. Ding, C. Shen, Z. Pan, D. Cuiuri, H. Li, N. Larkin, S. van Duin, Towards an automated robotic arc-welding-based additive manufacturing system from CAD to finished part, Computer-Aided Design 73 (2016) 66–75. doi:10.1016/j.cad.2015.12.003.

[35] R. J. Urbanic, R. W. Hedrick, C. G. Burford, A process planning framework and virtual representation for bead-based additive manufacturing processes, The International Journal of Advanced Manufacturing Technology 90 (1-4) (2017) 361–376. doi:10.1007/s00170-016-9392-8.

[36] E. Brandl, V. Michailov, B. Viehweger, C. Leyens, Deposition of Ti–6Al–4V using laser and wire, part I: Microstructural properties of single beads, Surface and Coatings Technology 206 (6) (2011) 1120–1129. doi:10.1016/j.surfcoat.2011.07.095.

[37] J. D. Spencer, P. M. Dickens, C. M. Wykes, Rapid prototyping of metal parts by three-dimensional welding, Proceedings of the Institution of Mechanical Engineers, Part B: Journal of Engineering Manufacture 212 (3) (1998) 175–182. doi:10.1243/0954405981515590.

[38] E. Sabourin, S. A. Houser, J. Helge Bøhn, Adaptive slicing using stepwise uniform refinement, Rapid Prototyping Journal 2 (4) (1996) 20–26.

[39] P. M. Pandey, N. V. Reddy, S. G. Dhande, Real time adaptive slicing for fused deposition modelling, International Journal of Machine Tools and Manufacture 43 (1) (2003) 61–71.

[40] J. S. Panchagnula, S. Simhambhatla, Manufacture of complex thin-walled metallic objects using weld-deposition based additive manufacturing, Robotics and Computer-Integrated Manufacturing 49 (2018) 194–203. doi:10.1016/j.rcim.2017.06.003.

[41] C. Dai, S. Lefebvre, K.-M. Yu, J. M. P. Geraedts, C. C. L. Wang, Planning jerk-optimized trajectory with discrete-time constraints for redundant robots, arXiv:1909.06570 [cs]arXiv:1909.06570.

[42] A. Liegeois, Automatic supervisory control of the configuration and behaviour of multibody mechanisms, IEEE Transactions on systems, man and cybernetics 7 (12) (1977) 868–871.

[43] A. Fournier, Génération de mouvements en robotique, applications des inverses généralisées et des pseudo-inverses, PhD Thesis, USTL, Montpellier (1980).

[44] C. A. Klein, Use of redundancy in the design of robotic system, robotics research, in: The Second International Symposium, Mit

Press, 1985, pp. 207–214.

[45] W. Khalil, E. Dombre, Modélisation, identification et commande des robots, Hermès science publ., 1999.

[46] J. Xiong, G. Zhang, J. Hu, L. Wu, Bead geometry prediction for robotic GMAW-based rapid manufacturing through a neural network and a second-order regression analysis, Journal of Intelligent Manufacturing 25 (1) (2014) 157–163. doi:10.1007/s10845-012-0682-1.

[47] T. Yoshikawa, Manipulability of robotic mechanisms, The International Journal of Robotics Research 4 (2) (1985) 3–9. doi:10.1177/027836498500400201.

[48] S. Zargarbashi, W. Khan, J. Angeles, The Jacobian condition number as a dexterity index in 6R machining robots, Robotics and Computer-Integrated Manufacturing 28 (6) (2012) 694–699. doi:10.1016/j.rcim.2012.04.004.

[49] M. Souissi, V. Hugel, S. Garbaya, J. Nassour, Minimized-torque-oriented design of parallel modular mechanism for humanoid waist, in: J. Lenarčič, J.-P. Merlet (Eds.), Advances in Robot Kinematics 2016, Vol. 4, Springer International Publishing, Cham, 2018, pp. 171–180. doi:10.1007/978-3-319-56802-7_18.

[50] A. Adebayo, J. Mehnen, X. Tonnellier, Limiting travel speed in additive layer manufacturing, in: 9th International Conference on Trends in Welding Research, Chicago, Illinois, USA, (2012).

[51] J. Xiong, R. Li, Y. Lei, H. Chen, Heat propagation of circular thin-walled parts fabricated in additive manufacturing using gas metal arc welding, Journal of Materials Processing Technology 251 (2018) 12–19. doi:10.1016/j.jmatprotec.2017.08.007.

[52] J. Yu, X. Lin, L. Ma, J. Wang, X. Fu, J. Chen, W. Huang, Influence of laser deposition patterns on part distortion, interior quality and mechanical properties by laser solid forming (LSF), Materials Science and Engineering: A 528 (3) (2011) 1094–1104. doi:10.1016/j.msea.2010.09.078.

[53] V. Ocelík, M. Eekma, I. Hemmati, J. De Hosson, Elimination of start/stop defects in laser cladding, Surface and Coatings Technology 206 (8-9) (2012) 2403–2409. doi:10.1016/j.surfcoat.2011.10.040.

[54] O. Yilmaz, A. A. Ugla, Development of a cold wire-feed additive layer manufacturing system using shaped metal deposition method, Journal of Mechanical Science and Technology 31 (4) (2017) 1611–1620. doi:10.1007/s12206-017-0308-9.

[55] S. Donadello, M. Motta, A. G. Demir, B. Previtali, Monitoring of laser metal deposition height by means of coaxial laser triangulation, Optics and Lasers in Engineering 112 (2019) 136–144. doi:10.1016/j.optlaseng.2018.09.012.

[56] D. Ding, Z. Pan, D. Cuiuri, H. Li, Wire-feed additive manufacturing of metal components: Technologies, developments and future interests, The International Journal of Advanced Manufacturing Technology 81 (1-4) (2015) 465–481. doi:10.1007/s00170-015-7077-3.

[57] W. U. H. Syed, A. J. Pinkerton, L. Li, Combining wire and coaxial powder feeding in laser direct metal deposition for rapid prototyping, Applied Surface Science 252 (13) (2006) 4803–4808. doi:10.1016/j.apsusc.2005.08.118.

[58] H. J. Woltring, Representation and calculation of 3-D joint movement, Human Movement Science 10 (5) (1991) 603–616.

[59] L. Boccaletto, Maîtrise du décollement de tuyère. Analyse du comportement d'une tuyère de type TOC et définition d'un nouveau concept: Le BOCCAJET, PhD Thesis, Université Aix-Marseille 1 (2011).

[60] C. Dordlofva, A. Lindwall, P. Törlind, Opportunities and challenges for additive manufacturing in space applications, DS 85-1: Proceedings of NordDesign 2016, Volume 1, Trondheim, Norway, 10th-12th August 2016 (2016) 401–410.

[61] P. R. Gradl, S. E. Greene, C. Protz, B. Bullard, J. Buzzell, C. Garcia, J. Wood, R. Osborne, J. Hulka, K. G. Cooper, Additive manufacturing of liquid rocket engine combustion devices: A summary of process developments and hot-fire testing results, in: 2018 Joint Propulsion Conference, American Institute of Aeronautics and Astronautics, Cincinnati, Ohio, 2018. doi:10.2514/6.2018-4625.